Lasers in Manufacturing Conference 2023

High resolution ultrashort UV pulsed laser processing with parallel Bessel beams for cylinder tooling

Stephan Buening[a,*], Martin Osbild[b], Keming Du[c], Arnold Gillner[b]

[a]Schepers GmbH & Co. KG, Karl-Benz-Straße 7, 48691 Vreden, Germany
[b]Fraunhofer Institute for Laser Technology (ILT), Steinbachstr. 15, Aachen, 52074, Germany;
[c] Edgewage GmbH, Carlo-Schmid-Straße 19, 52146 Würselen, Germany

Abstract

Micro structuring with ultrashort laser pulses in the UV wavelength range makes it possible to create surface structures in the sub micrometer range on rotating tools that lead to specific functional properties. To transfer these functionalities from the tool to large surfaces (e.g. foils), a roll-to-roll nanoimprint application is the most efficient method, as processing speeds of up to 20 m² per min are possible.

This paper presents the optical setup of a laser structuring machine that uses four parallel Bessel beams. Each beamlet can be modulated individually to allow flexible generation of arbitrary surface structures. Ablation results with structure sizes of 1 µm are presented. A strategy for estimating the position-dependent peak fluence based on CMOS images of the Bessel beam along the propagation has been developed. In addition, a novel approach for lateral Bessel beam scanning for efficient machining of cylinders based on RF shifting in AODs is presented in this paper.

Keywords: Bessel beam; ultrafast laser; ultra-short pulse laser; micro structuring; nano structuring

1.   Motivation

In the literature, structured surfaces in the micro or nano range are described with numerous functional properties. The functionality is essentially defined by the size and shape of the structure, which for these structures are described by pixel sizes <1 µm. In order to be able to transfer digital structures to surfaces, tool geometries of 1 µm and smaller are also necessary. This is where the Gaussian focusing of ultra-short pulsed laser radiation reaches its limits. The extremely high resolutions result in extremely long process times. Here, the use of many parallel ultra-short pulsed laser spots has become established and is important for a wide field of applications in micromachining when it comes to large components with dimensions of >> 1 m². By controlling the laser beam with appropriate precision, virtually any structure can be written directly. However,

focusing on diameters of 1 µm and smaller with a Rayleigh range suitable for material processing has so far been a challenge.

When small processing diameters with large depth of focus are necessary, Bessel beams have found a range of applications in material processing. These beams are non-diffractive, which allows for the creation of spot sizes in the sub-micron range with an independent depth of focus of several millimeters. Bessel beams are often used to process transparent materials, such as in glass cutting[1] or the fabrication of nanochannels in glass[2, 3], due to their extreme aspect ratios. However, they can also be used for surface structuring of non-transparent materials when extremely small spot sizes are needed. The large focal plane tolerance of Bessel beams is particularly useful for rough or uneven surfaces or when the positioning accuracy of the machine is limited in the z-direction[3–5].

Bessel beam ablation is most effective when the beam is stationary while the workpiece performs the relative movement instead. However, linear axes for precise laser processing have maximum velocities of less than 1 m/s. In contrast, cylinder structuring machines can reach surface speeds of up to 50 m/s, making them suitable for ultrafast Bessel beam ablation using high power at high repetition rates. Even though repetition rates in the multiple MHz range can be used with a 1 µm spot, the resulting ablation rates are still too low for economic industrial use. Consequently, it is particularly interesting to combine Bessel beam ablation with multi-beam technology, as presented in this work.

1.1 State of the art

In a previous study[7,8] two optical setups for sub-micron laser ablation using single Bessel beams. A conventional refractive axicon and an innovative reflective axicon were used to generate the respective primary Bessel profile, which was then demagnified by a 4f-arrangement that is the same one as in this paper. The lens pair in the 4f-arrangement decreases the radial and axial dimensions of the Bessel core[9]. The generation of a smaller secondary Bessel profile is often preferred in material processing as it leads to a higher energy density and a larger working distance. The feasibility of sub-micron surface structuring with both axicons using linear axes motion were shown. It demonstrates that the quality of both Bessel beams was good, as evidenced by their agreement with the theoretical intensity curve. Heavy on-axis oscillations of the intensity as a result of an imperfect tip as commonly found in literature[6, 10, 11] could not be observed. The intensity measurements and ablation results of the Bessel beam generated by the reflective axicon are shown in Fig. 1.
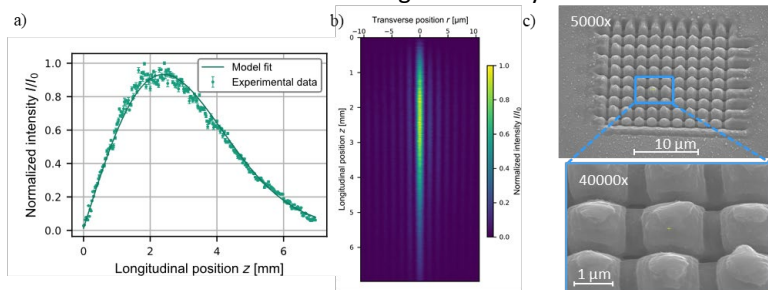

Fig. 1. Results from single Bessel beam experiments conducted in a previous study[8] using the same laser source and optics as in this paper. a) The measured on-axis intensity evolution along the Bessel beam propagation follows the theoretical model closely. b) A colored 2D plot of intensity distribution of the Bessel beam illustrates the high aspect ratio. c) A scanning electron microscopy (SEM) image of a crosshatch structure with 0.4 µm wide grooves machined using the Bessel beam.

This paper mainly presents the transfer of the single Bessel beam setup used in the laboratory, which consists of a refractive axicon with a 5° base angle (170° apex angle), an f = 75 mm plano-convex lens, and an f =

25 mm asphere, to a multibeam setup for cylinder structuring in an industrial environment. The topic of cylinder structuring strategies and a practical methodology for characterizing Bessel beams will also be covered.

2. Multiscan technique in cylinder processing

2.1 *Process strategies for laser structuring of cylinders*

To achieve highly economical laser structuring of cylinder surfaces, the tool slide simply moves continuously along the length of a rotating cylinder. The result is a spiral feed and a process time reduced by a factor of 2.5 compared to a block feed application.

Due to its principle, a spiral feed comes with the inherent difficulty that no exact circumferential line can be machined. The starting and end point of a circumferential line are shifted against each other according to the axial feed per cylinder rotation since the tool slide moves continuously. This would result in a visible seam, which is unacceptable in most applications. In addition, the processing time for a cylinder usually ranges from a few hours to several days. The process is subject to some disturbance factors such as temperature changes or vibrations. In many cases, the expansion effects are tolerable. However, at high resolutions with small spot diameters, this can lead to poor machining quality.

To overcome this challenge of axial inaccuracies, that are particularly critical in multilayer engraving, it is necessary to perform the entire machining of the cylinder in a single pass. This means that the tool slide may only be moved once from the beginning to the end of the cylinder. The process is also based on the ability to position the laser spot axially on the cylinder in a defined area. The tracks are machined multiple times, but from different axial positions of the focus head, using beam deflection through RF shifting. This so-called Multiscan technique makes it possible to produce a uniform engraving image from start to finish, even with large cylinder widths. Fig. 2 shows the principle of Multiscan in a schematic drawing.
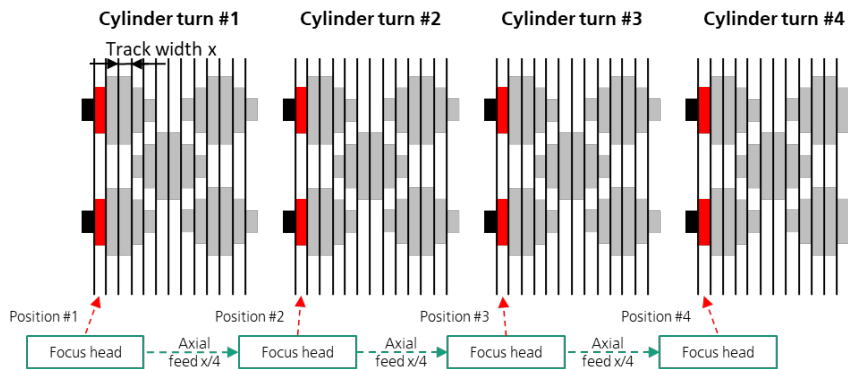

Fig. 2. Illustration of the Multiscan technique. Four layers of the second track are machined despite the continuous movement of the focus head.

2.2 *Multiscan technique for Bessel beams*

The Multiscan process strategy shall also be used for Bessel beam machining. Especially with laser spots of around 1 µm, the complete structuring of the cylinder must be ensured in one pass since the slightest axial inaccuracies would be directly noticeable. The approach is the same as for conventional Gaussian beams:

shifting the radio frequency of the AOM changes the incident angle on the axicon. The subsequently generated Bessel beam also possesses an oblique propagation direction. Thus, a lateral displacement is induced with a magnitude dependent on the longitudinal position of the processing plane. The presence of a demagnifying optical system influences the Bessel beam propagation but does not hinder it. Studies treating the oblique illumination of axicons imply that the Bessel profile with the high-intensity central lobe persist for small angles <1°. Larger illumination angles lead to a checkerboard pattern that cannot be used for micro and nano structuring[12–15]. A schematic drawing about the Bessel beam scanning for cylinder structuring is shown in 3. A further limitation arises from the requirement that the input beam has to sufficiently illuminate the axicon's apex.

For designing an optical system, it is advantageous to know the influence of the applied RF signal of the AOM on the resulting deflection angle. For an efficient deflection, the incident laser beam at the AOM must have a certain angle relative to the acoustic wave propagation in the AOM crystal, which is known as Bragg angle. The separation angle between the deflected first order beam and the transmitting zeroth order beam is given by the equation[16].

$$\theta = \frac{\lambda \cdot f_{RF}}{n \cdot v_{sound}} \tag{1}$$

where λ is the laser wavelength, n is the refractive index of the AOM crystal, f_{RF} is the applied radio frequency, which is also the acoustic frequency in the AOM crystal, and v_{sound} is the material-dependent wavelength of sound. The Bragg condition covers a small frequency range. This can be observed very well by the fact that the optical deflection efficiency decreases if the deviation of the angle or RF is too large. To know the angle of incidence at the Axicon $\Delta\theta$ for a changed RF signal $f_{RF,shifted}$, the difference between the separation angles of the original frequency $\theta\left(f_{RF,orig}\right)$ and the shifted frequency $\theta\left(f_{RF,shifted}\right)$ has to be calculated:

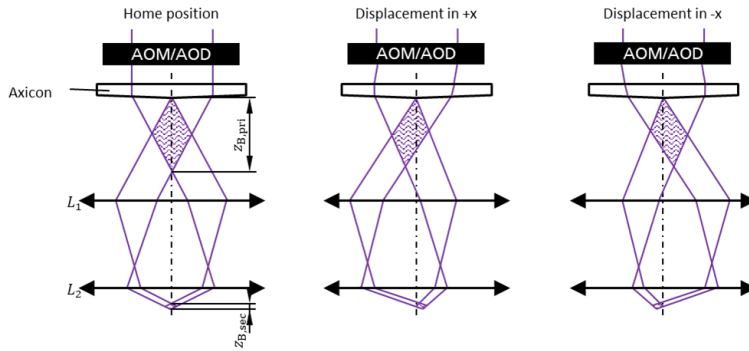$$\Delta\theta = \theta\left(f_{RF,orig}\right) - \theta\left(f_{RF,shifted}\right). \tag{2}$$

Fig. 3. Principle of Bessel beam scanning using RF shifting in an AOM/AOD. The Bessel beam can be scanned in one dimension in both directions from the original position.

3. Experimental setup

The experiments were carried out with the high precision cylinder processing system Digilas. The schematic setup is shown in Fig. 4. The entire beam path, including the beam source, is mounted on a breadboard that

moves parallel to the axis of the cylinder. An ultrafast laser beam source with a wavelength of λ = 343 nm, a maximum pulse energy of E_P = 6 µJ at a pulse repetition rate of f_{rep} = 5 MHz, a pulse duration of τ = 400 fs and a raw beam diameter ($1/e^2$) of 3 mm is used. To prevent clipping at the apertures of the acousto-optic modulators (AOM), the raw beam is reduced to 2/3 of its original size in a Kepler telescope consisting of two plano-convex lenses. This arrangement was chosen over a Galilei telescope due to less sensitive beam alignment requirements. Four beamlets with equal power were then generated in the beam splitting unit, which consists of three non-polarizing plate beam splitters and several mirrors. Each beamlet passes through a single-channel AOM, which allows for the individual modulation of each beamlet. The zeroth-order beam is stopped from further propagation in a water-cooled beam dump. Only the beams deflected by the AOM can enter the refractive axicons to form a primary Bessel profile.

To minimize the distance between adjacent Bessel beams, we used UV-compatible half-inch axicons to fit within the given machine. As aforementioned, the primary Bessel beam is demagnified by a f = 75 mm plano-convex lens and a f = 25 mm asphere in a 4f-arrangement as shown in detail in Fig. . The polished copper surface of the sample cylinder is positioned within the secondary Bessel profile.
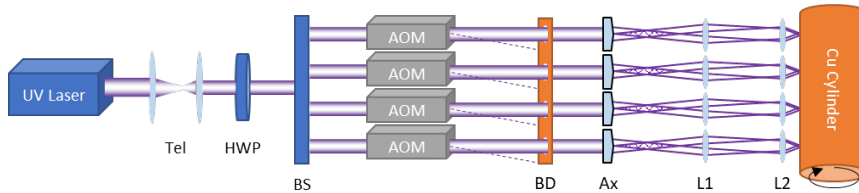

Fig. 4. Schematic of the experimental setup on a cylinder structuring machine. For clarity, deflection mirrors are not shown. The ultrashort pulsed UV laser beam is first demagnified in a Kepler telescope (Tel), then guided through a half-wave plate (HWP) and split into four beamlets in the beam splitting unit (BS). Each beamlet propagates through an AOM. The zeroth order beams (dashed line) are directed into a beam dump (BD). The Bessel beams are then formed by a refractive axicon (Ax) and a lens pair in a 4f-arrangement (L1+L2).
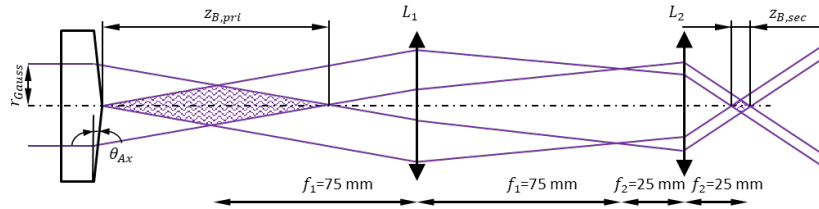

Fig. 5. Magnified schematic of the Bessel beam generation. The primary ($z_{B,pri}$) and secondary ($z_{B,sec}$) Bessel beam are shown. The same indices will also be used for the Bessel core radii ($r_{B,pri}$ and $r_{B,sec}$).

4. Experimental results

4.1 Ablation results

Diamond-shaped patches consisting of lines and dots were microstructured on the copper surface of the sample cylinder, with line and dots width of approximately 1 µm. Fig. 6 shows the underlying microscope images. The single-pass structure was carried out at an average power of P_{av} = 3 W and a repetition rate of f_{rep} = 5 MHz. The surface speed was 5 m/s for the line structure and 10 m/s for the dot structure. The experiments were repeated for multiple z-positions with similar results, which showed the robustness of Bessel beam ablation.
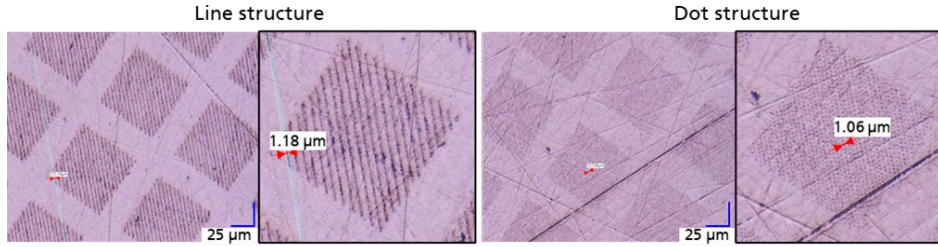
Fig. 6. Ablated line and dot structures of approximately 1 µm on a polished copper cylinder demonstrate the high resolution of Bessel beam micro machining.

4.2   Scanning of the Bessel beam

The AOM's base frequency is 110 MHz and the slightly divergent input beam on the axicon is approximately 3 mm in diameter. The RF range of the AOM is varied between 100 MHz and 120 MHz. Fig. shows the intensity profiles of the scanned Bessel beam with respect to the applied RF signal. Within this RF range, the Bessel profile preserves its concentric shape, but there is also a decreasing intensity of the Bessel core the farther the deviation from the base RF is. The achievable lateral travel range depends on the longitudinal position of the observation or processing plane, respectively. The largest scanning range that could be identified in this setup was 3.5 µm.
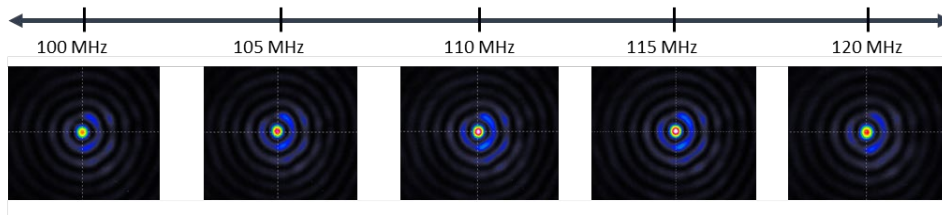

Fig. 7. Beam profiles recorded in the single beam setup at Fraunhofer ILT.

The AOM crystal consists of crystal quartz with a refractive index of n = 1.55 and a speed of sound of v_{sound} = 5750 m/sKlicken oder tippen Sie hier, um Text einzugeben.[17]. Inserting the varied radio frequencies in eq. (1) yields the separation angles θ. From these results the angle of incidence at the axicon can be calculated according to eq. (2). Table 1 shows that the corresponding angles of incidence for a well-shaped Bessel beam are extremely small.

Table 1. Summary of calculated separation and incidence angles.

RF f_{RF} [MHz]	Separation angle θ [mrad]	Separation angle θ [°]	Angle of incidence at the axicon $\Delta\theta$ [°]
100	3,98	0,228	-0,0228
105	4,18	0,240	-0,0114
110 (base RF)	4,38	0,251	0,0000
115	4,58	0,262	0,0114
120	4,78	0,274	0,0228

5. Charactarization of the Bessel Beam

5.1 Methodology

Images of the Bessel profile in the focal plane of the microscope objective are acquired slice by slice along the propagation axis by moving the z positioning stage in 100 µm increments from the start to the end of the Bessel zone, with five images taken from each plane. In the post-processing for every single image, the first step of the algorithm involves extracting the area of interest by detecting the central pixel of the intensity peak. The row and column (x- and y-direction, respectively, see Fig. 8a of the pixel matrix with the detected central pixel as intersection are then plotted on separate two-dimensional graphs with the grayscale values of each pixel as the ordinate and the pixel position on the abscissa. After that, a Gaussian fit is performed on the center of these plots (ideally, the central lobe of a Bessel intensity distribution), as illustrated in Fig. 8b. From this fit, the maximum relative intensity and the Bessel core radius r_B defined as the radius at which the intensity falls to $1/e^2$ of its maximum are calculated. The results from the five images taken at each plane are used to determine the mean values and standard deviations for each z-position in both the x- and y-direction. It is important to consider the values in both directions separately, as differences between them may indicate a distorted beam profile.
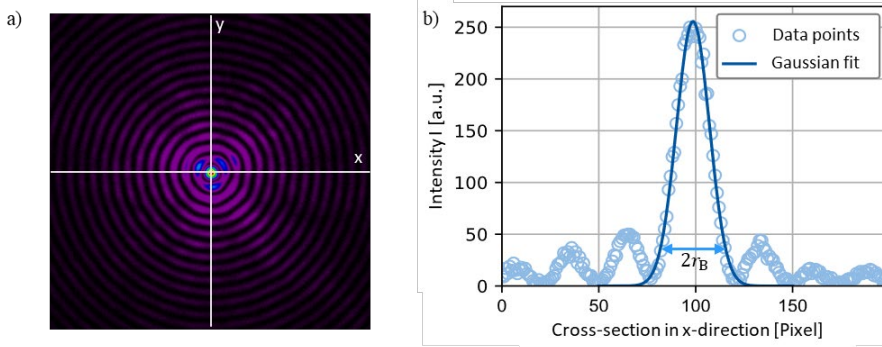

Fig. 8. Example for an intensity-dependent false color image of the Bessel beam cross-section and the corresponding Gaussian fit of the central lobe in x-direction. The relative peak intensity and the $1/e^2$-Bessel radius r_B are taken from the Gaussian fit in both x- and y-direction.

It is crucial to have a rough knowledge of the peak fluence F_0 when using ultrafast lasers for material processing. This is because material-specific process knowledge is often recorded using the fluence as an input parameter. In addition, when using Bessel beam ablation, there are limits on the fluence that can be applied, as the first side lobe contains 16% of the fluence of the central core. By knowing the fluence in the Bessel beam, it is possible to determine whether the side lobe will also ablate the material based on the material's threshold fluence. In the following, we present the derivation of a formula for the fluence curve $F_0(z)$ that can be determined solely from laser beam source parameters and beam profiling results.

For Bessel-Gauss beams, the on-axis peak fluence over the propagation length is described by the following equation for a collimated input beam[6]:

$$F_0(z) = \frac{4 P_{av} k}{f_{rep}} \cdot \cos\left(\frac{1.75}{k \cdot r_B}\right) \cdot \frac{z}{z_B^2} \cdot e^{-2z^2/z_B^2}. \tag{9}$$

The parameters f_{rep} and k are usually known and P_{av} can be measured directly with a power meter placed behind the last optic (L2 in this case). The parameters that need to be derived from camera-based beam

characterization are the Bessel core radius r_B and the length of the Bessel zone z_B. The best strategy for obtaining these parameters is discussed in the following section.

As depicted in Fig. 1a and described in the previous study[8], the curve of the intensity (in arbitrary units) along the Bessel beam propagation $I_0(z)$ can be fitted by the simplified function

$$I_0(z) = A \cdot z \cdot e^{-B \cdot z^2} + C. \tag{10}$$

The longitudinal position of the intensity maximum z_peak can be determined by setting the derivative of function (8), $I_0^{'}(z)$, equal to zero. This results in the following equation for z_peak:

$$z_\text{peak} = \frac{1}{\sqrt{2B}}. \tag{11}$$

We use the definition[11]

$$z_\text{B} = 2z_\text{peak} \tag{12}$$

to obtain the length of the Bessel zone. To determine a representative value for the Bessel core radius r_B, we recommend to use the mean value of the radii within a narrow corridor around the intensity peak z_peak because the radius tends to be unstable near the start and the end of the Bessel zone.

Once the Bessel beam parameters describing the Bessel profile in radial and longitudinal direction are known, a simple proportionality between the maximum peak fluence and the measured average power can be established. This allows for a convenient estimation of the maximum usable power without ablation from the side lope. By setting $z = z_\text{peak} = z_\text{B}/2$ from eq. (12) in $F_0(z)$ from eq. (9), we obtain:

$$F_{0,\max} = P_\text{av} \cdot \left[\frac{2k}{f_\text{rep} \cdot z_\text{B}} \cdot \cos\left(\frac{1.75}{k \cdot r_\text{B}}\right) \cdot e^{-\frac{1}{2}} \right]. \tag{13}$$

5.2 Results

Fig. 9. shows the fitted Bessel radii $r_\text{B,sec}$ in x- and y-direction as well as the weighted mean value from the slice-by-slice analysis described in the previous Chapter 5.1. Please note that this is an imperfectly aligned Bessel beam to demonstrate that the algorithm is also useful in non-ideal real-world cases. In such cases, the usable length of the Bessel beam for microstructuring is reduced from > 3 mm to around 1 mm. A good indicator of a functional Bessel beam is the congruence of the radii in x- and y-direction. If the radii differ, it is likely that the beam profile is distorted, possibly taking the form of a checkerboard pattern or a vanishing Bessel beam.

Fig. 10a shows the normalized on-axis intensity along the Bessel beam propagation. The fitted curve, which follows the function (10), is in good agreement to the experimental data points. The biggest deviation occurs in the vicinity of the peak intensity, which may be caused by the divergence of the input beam. The z-position of the peak is $z_\text{peak} = 1.64$ mm and can be determined from the fit, and therefore also the length of the Bessel beam $z_\text{B,sec}$ according to equation (12)[11]. The algorithm calculates the mean of the discrete radii around the peak within ±250 µm and defines the result as $r_\text{B,sec}$, which amounts to 0.92 µm in this setup. Using $z_\text{B,sec}$ and $r_\text{B,sec}$, as well as the remaining laser parameters and equation (7), it is possible to calculate the on-axis fluence curve along the Bessel beam propagation. Despite the small spot size, the estimated maximum reachable peak fluence is $F_{0,\max} = 0.67$ J/cm² for an exemplary moderate power of 5 W per beamlet. As a reference, the

threshold peak fluence of copper using ultrafast UV lasers is about F_{thr}=0.1 J/cm[22]. Consequently, this peak fluence at $P_{av} = 5$ W is already approximately the upper limit, so no ablation is induced by the side lobe. For the 30 W UV laser source used in the experiment, 5 W is also approximately the upper power limit that one of the four beamlets can contain due to losses in the optics especially in the zeroth order after the AOMs.
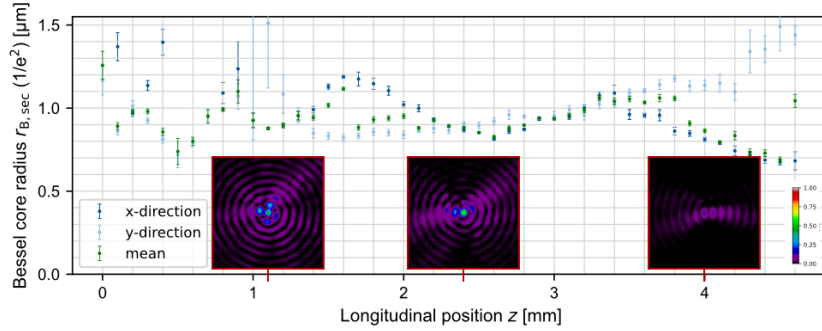

Fig. 9. The Bessel core radius was measured in both the x- and y-directions along the beam propagation. The mean was calculated by weighting the radius in the x- and y-directions based on the errors. Deviations from radial symmetry were observed due to imperfect alignment of the Bessel beam. It can be assumed that the closer the radii in the x- and y-directions are to each other, the better the cross-sectional profile of the Bessel beam is at a given point. The three false-color plots show the Bessel profile at z-positions of 1.1 mm, 2.4 mm, and 4.0 mm, respectively.
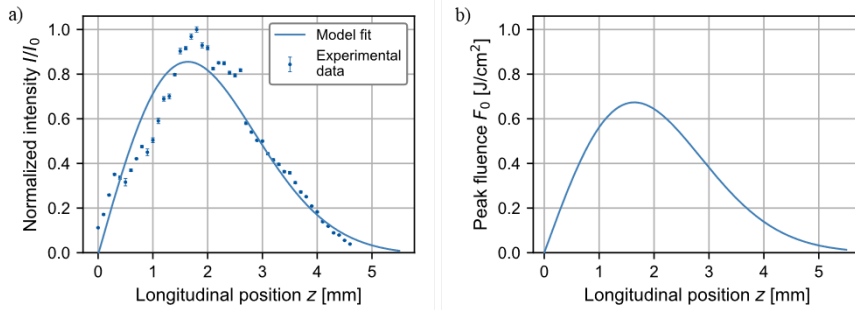

Fig. 10. Diagram a) shows the normalized on-axis intensity along the Bessel beam propagation and the corresponding curve fitting using equation (10). Diagram b) shows the on-axis peak fluence over the longitudinal position according to equation (9) for an average power of 5 W in each beamlet.

6.   Conclusion

For microstructures <1 μm, the system described here has shown great promise for use with cylindrical laser processing machines for tool processing. An ultrafast UV laser source (343 nm) was split into four paths, each one individually modulated, could be modulated and shaped by a conventional refractive axicon and a demagnifying lens pair arranged in a 4f configuration. We have presented a strategy for efficient and accurate cylinder patterning using a spiral feed and the ability of the Gaussian beam to be scanned laterally using RF shifts in the AOMs. This strategy can also be used to pattern Bessel beams, provided the input raw beam at the axicon is large enough. Furthermore, a camera-based method for characterizing real-world Bessel beams is presented, which allows for the estimation of the position-dependent fluence $F_0(z)$ even if the properties of the input beam at the axicon are unknown. Overall, this optical system represents a significant advance in the field of laser cylinder structuring, especially for small structures.

Acknowledgement

References

[1] Lopez, J., Mishchik, K., Chassagne, B., Javaux-Leger, C., Hönninger, C., Mottay, E. and Kling, R., "Glass cutting using ultrashort pulsed bessel beams,", 60–69 (October 18–22, 2015).

[2] Duocastella, M. and Arnold, C. B., "Bessel and annular beams for materials processing," Laser & Photon. Rev. 6(5), 607–621 (2012).

[3] Courvoisier, F., Zhang, J., Bhuyan, M. K., Jacquot, M. and Dudley, J. M., "Applications of femtosecond Bessel beams to laser ablation," Appl. Phys. A 112(1), 29–34 (2013).

[4] Michalowski, A., Freitag, C., Weber, R. and Graf, T., "Laser surface structuring with long depth of focus," SPIE Proceedings, 79200W (2011).

[5] Kumar, S., Eaton, S. M., Bollani, M., Sotillo, B., Chiappini, A., Ferrari, M., Ramponi, R., Di Trapani, P. and Jedrkiewicz, O., "Laser surface structuring of diamond with ultrashort Bessel beams," Scientific reports 8(1), 14021 (2018).

[6] Brzobohatý, O., Cizmár, T. and Zemánek, P., "High quality quasi-Bessel beam generated by round-tip axicon," Opt. Express 16(17), 12688–12700 (2008).

[7] J. Durnin, J. J. Miceli, Jr. and and J. H. Eberly, "Diffraction-free beams," (1987).

[8] Osbild, M., Gerhorst, E.-A., Sivankutty, S., Pallier, G. and Labroille, G., "Submicrometer surface structuring with a Bessel beam generated by a reflective axicon," Journal of Laser Applications 33(4), 42013 (2021).

[9] Dudutis, J., Stonys, R., Račiukaitis, G. and GeČys, P., "Aberration-controlled Bessel beam processing of glass," Optics express 26(3), 3627–3637 (2018).

[10] Akturk, S., Zhou, B., Pasquiou, B., Franco, M. and Mysyrowicz, A., "Intensity distribution around the focal regions of real axicons," Optics Communications 281(17), 4240–4244 (2008).

[11] Wu, P., Sui, C. and Huang, W., "Theoretical analysis of a quasi-Bessel beam for laser ablation," Photon. Res. 2(3), 82 (2014).

[12] Arimoto, R., "Imaging properties of axicon in a scanning," Applied optics (31), 6653-6657 (1992).

[13] Bin, Z. and Zhu, L., "Diffraction property of an axicon in oblique illumination," Applied optics 37(13), 2563–2568 (1998).

[14] Tanaka, T. and Yamamoto, S., "Comparison of aberration between axicon and lens," Optics Communications 184(1-4), 113–118 (2000).

[15] Thaning, A., Jaroszewicz, Z. and Friberg, A. T., "Diffractive axicons in oblique illumination: analysis and experiments and comparison with elliptical axicons," Applied optics 42(1), 9–17 (2003).

[16] AA Opto-Electronic, "Do you know Acousto-optics? Application Notes,", http://www.aaoptoelectronic.com/wp-content/uploads/documents/AA-THEORY-NOTES.pdf (10 January 2023).

[17] Gooch & Housego, "Introduction to AO Modulators and Deflectors,", https://www.optoscience.com/maker/gooch/pdf/IntroductionAO.pdf (10 January 2023).

[18] Hodgson, N., Steinkopff, A., Heming, S., Allegre, H., Haloui, H., Lee, T., Laha, M. and VanNunen, J., "Ultrafastmachining: process optimization and applications,", 6 (06.03.2021 - 12.03.2021).